

Cosmological structure formation and ripples of dark energy

Nicolò Massari

Supervisors:

Julian Adamek

Lavinia Heisenberg

Francesca Lepori

November 23, 2023

1 Introduction

This report investigates the influence of varying dark energy sound speeds (c_s^2) with an equation of state parameter (w) close to -1 on the development of large-scale cosmic structures. Through computations with the Boltzmann code: *CLASS* (Lesgourgues, 2011), and simulations with the N-body code: *gevolution* (Adamek et al., 2016), we explore different c_s^2 values: 1, 10^{-4} , 10^{-7} , and 0. In contrast to the traditional Λ CDM model, our approach adopts a reference cosmology with $w = -0.8$ and $c_s^2 = 1$.

The analysis focuses on two core observables: the matter density power spectrum and its respective correlation function. To quantify the deviations due to sound speed variations, percentage difference plots are presented relative to the aforementioned reference cosmology.

The structure of this report is as follows: Section 2 provides a theoretical backdrop, emphasizing the significance of sound speed variations. Section 3 delineates the methodology utilizing the *CLASS* and *gevolution* codes, accompanied by parameter specifications. In Section 4, the findings are presented, encompassing matter density power spectra, cor-

relation functions, and percentage difference plots. Conclusion and acknowledgements are presented in Section 5.

2 Dark energy perturbations

From Batista's review (Batista, 2021) on clustering dark energy we can find how strongly the dark energy perturbations depend on the choice of w and c_s .

Assuming w and c_s constant, we find this second-order equation for dark energy:

$$\begin{aligned} \delta_{\text{de}}'' + H(1 - 3w)\delta_{\text{de}}' + [3H'(c_s^2 - w) + 3H^2(c_s^2 - w)(1 - 3c_s^2) + c_s^2 k^2] \delta_{\text{de}} \\ = -(1 + w)[k^2 \Phi - 3H(1 - 3c_s^2)\Phi' - 3\Phi'']. \end{aligned} \quad (1)$$

Assuming small scales $k^2 \gg H^2$, H' , and the matter-dominated solution $\delta_m \propto a$ and $\Phi = \text{constant}$, simplifies equation (1) to

$$\delta_{\text{de}}'' + H(1 - 3w)\delta_{\text{de}}' + c_s^2 k^2 \delta_{\text{de}} = -(1 + w)k^2 \Phi. \quad (2)$$

For non-negligible c_s , equation (1) has a constant solution:

$$\delta_{\text{de}} = -\frac{(1 + w)}{c_s^2} \Phi, \quad (3)$$

solution applicable for $c_s^2 = 1$.

For negligible c_s , equation (1) has the following solution:

$$\delta_{\text{de}} = -\frac{(1 + w)}{1 - 3w} \delta_m, \quad (4)$$

which is the solution we are most interested in when using values for $c_s^2 = 10^{-4}, 10^{-7}$, and 0. Plugging our simulation value for the state parameter $w = -0.8$, equation (4) becomes:

$$\delta_{\text{de}} \sim -0.06 \delta_m. \quad (5)$$

Another notable prediction from theory is that DE perturbations will be strongly suppressed below the sound horizon (Appendix 6.1):

$$\chi_{sh} = c_s \chi_h = c_s \int_{a_i}^1 \frac{da}{a^2 H}, \quad (6)$$

In regions below this scale, the pressure support halts the growth of DE perturbations. Quintessence models have $c_s = 1$; then, $\chi_{sh} \sim \chi_h \sim 1/H_0$, and their perturbations are very small on scales below the Hubble radius. We anticipate that perturbations will fall around

the sound horizon. On scales smaller than the sound horizon, structures are expected to closely resemble the $c_s = 1$ case. Furthermore there are no significant constraints on the sound speed parameter, allowing for the exploration of k-essence models with $c_s \ll 1$ (Planck Collaboration, 2016, sec 5.3.1.).

2.1 LCDM vs $w = -0.99$ vs $w = -0.8$

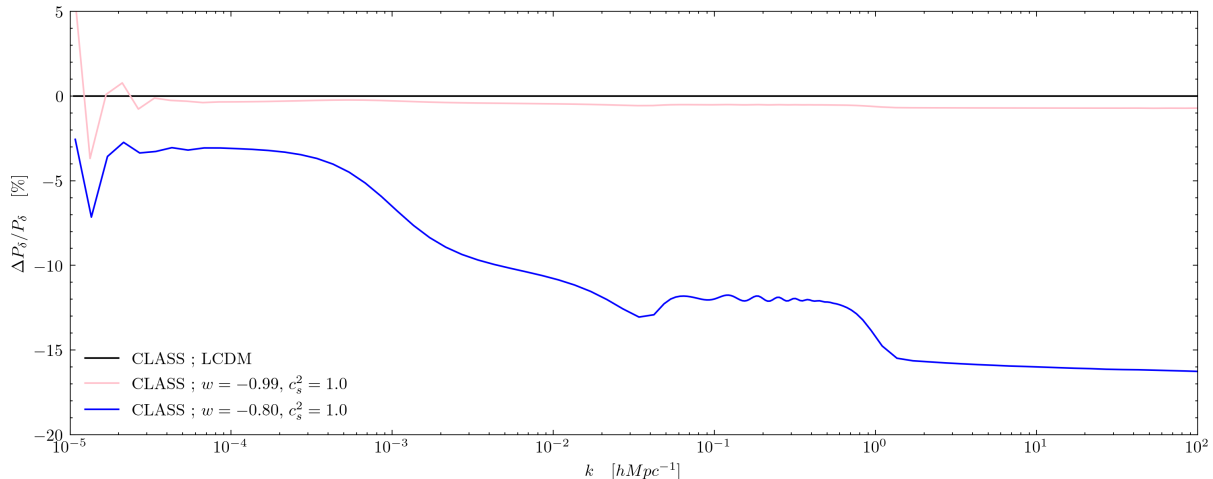


Figure 1: Percentage difference plots of the matter power spectra with respect to the LCDM just by varying the value of w to -0.99 and -0.8

Choosing a value for the equation of state parameter (w) that deviates significantly from -1 holds consequences. For example we know from both equation (3) and (4) that DE perturbations grow with $|1 + w|$. Moreover, as depicted in Figure 1, a change in the state parameter has a direct effect on the matter power spectrum, which is of smaller amplitudes with a lower w . Since plots are given by:

$$\Delta P_\delta / P_\delta = 100 \frac{P_{\delta, w=-0.99, -0.8} - P_{\delta, w=-1}}{P_{\delta, w=-1}}. \quad (7)$$

3 Methods

3.1 CLASS vs *gevolution*

In our study, we employ two key computational frameworks, *CLASS* (Cosmic Linear Anisotropy Solving System) and *gevolution* (General Relativistic N-body Code).

CLASS is a so called Boltzmann code, much like CMBFAST, CAMB and CMBEASY. A Boltzmann code is any code that gives a numerical solution of the Einstein-Boltzmann equations. This set of first-order linear homogeneous differential equations excels in modeling early Universe perturbations and is a powerful tool for predicting cosmic microwave background (CMB) anisotropies, as well as the matter power spectrum, within the linear regime.

gevolution a particle-mesh (PM) N-body code which is specifically designed to provide a general relativistic (GR) treatment of gravity. It therefore specializes in capturing non-linear interactions. In particular it uses *CLASS* to compute the values of the transfer functions $T(k)$ up to a certain redshift z for each of the main perturbation fields: e.g. ϕ , δ , u , δ_b , u_b , θ_0 , θ_1 , N_0 , N_1 , N_2 .

3.2 Simulation parameters

The *gevolution* code allows the user to use the same parameters (.ini) file to run both *gevolution* and *CLASS*. The initial conditions parameters for the cosmology used result as follows:

```

1 A_s = 2.1e-9
2 k_pivot = 0.05
3 n_s = 0.96
4 h = 0.67
5 omega_cdm = 0.121203
6 omega_b = 0.021996
7 Omega_fld = 0.6795281413370983
8 T_cmb = 2.7255
9 m_ncdm = 0.00868907, 0.05
10 N_ncdm = 2
11 T_ncdm = 0.71611080535681526325444872500459
12 N_ur = 1.0196
13 w0_fld = -0.8
14 wa_fld = 0.
15 cs2_fld = 1    #10e-4, 10e-7, 0

```

where the parameter `cs2_fld` has been equaled 1, 10^{-4} , 10^{-7} , and 0. Furthermore the cosmological parameters have been chosen to fit k-essence models examined in Hassani,

Adamek, Kunz’s publication ([Hassani et al., 2023](#)).

3.3 *gevolution* parameters

Regarding the *gevolution* simulation runs there were some computational power constraints, due to limited access of ETH’s Euler cluster ¹. `boxsize` is quite small but necessary for a good resolution, we discuss further tests on `boxsize` values in section 4.2. The number of particles in each run is given by:

$$N = N_{template} \cdot T^3 = 64 \cdot 96^3 = 384^3 \sim 6 \times 10^7, \quad (8)$$

where T is the tiling factor and $N_{template}$, given by the `sc1_crystal.dat` cubic template, is 64 particles total, a 4x4x4 crystal.²

```
1 template file = sc1_crystal.dat
2 tiling factor = 96, 0, 0
3 boxsize = 640.0
4 Ngrid = 384
5 Courant factor = 48.0
6 time step limit = 0.04
7
8 seed = 42
9 IC generator = basic
10 gravity theory = GR
11 vector method = parabolic
12 correct displacement = yes
13 k-domain = sphere
14 baryon treatment = blend
15 radiation treatment = CLASS
16 fluid treatment = CLASS
17 initial redshift = 100.0
```

Four different simulations have been run for every value of sound speed, varying the value of `seed`= 42, 43, 44, 45. The power spectrum data showed in this report and used to

¹[Euler Cluster](#)

²[gevolution manual](#)

obtain the correlation function, for each sound speed, is then the average resulted from these runs.

3.4 *CLASS* parameters

Additional *CLASS* parameters different from default:

```
1 P_k_max_h/Mpc = 192
```

4 Results

4.1 Power Spectrum

The top panel of Figure 2 doesn't distinguish between different sound speeds as the percentage difference across all cases is less than 2%, which would not be visible on the $P_\delta(k)$ plot. Instead we show the deviation from $c_s = 1$ in the bottom panel of Figure 2. The power spectra obtained with *gevolution* has been handled to create a smooth integrable function on which to perform a Fourier transformation to obtain a correlation function. This smooth power spectrum, shown in pink in Figure 2, uses *CLASS* data up to $k \sim 0.06 h Mpc^{-1}$, then interpolated *gevolution* data up to $k \sim 1.4 h Mpc^{-1}$ and finally an extrapolation has been performed for larger k 's. As expected *gevolution* recreates the main feature of the non linear power spectrum, a higher clustering at non linear scales.

Plots showed in the bottom panel of Figure 2 are obtained using the following formula:

$$\Delta P_\delta / P_\delta = 100 \frac{P_{\delta, c_s^2=1} - P_{\delta, c_s^2=10^{-4}, 10^{-7}, 0}}{P_{\delta, c_s^2=1}}. \quad (9)$$

As explored in (de Putter et al., 2010), in models where w is allowed to be different than -1, the sound speed of DE should have a noticeable influence on structure formation. *CLASS* plots for $c_s^2 = 10^{-4}, 10^{-7}$ follow $c_s = 0$ for modes $k \ll k_{sh}$. For $k \gg k_{sh}$, perturbations are killed off and plots start following $c_s = 1$. As expected we do observe a very keen agreement of $c_s^2 = 10^{-7}$ with $c_s = 0$ up to the sound speed horizon. One can see that for $c_s^2 = 10^{-4}$, *gevolution* follows *CLASS* very closely up to a certain k but then it plateaus at a difference of around 0.3%. For $c_s^2 = 10^{-7}$ we don't observe this agreement with *CLASS*, with discrepancies over 1% for higher k 's. To explain this anomaly we have run a few tests varying the `boxsize` in our simulations.

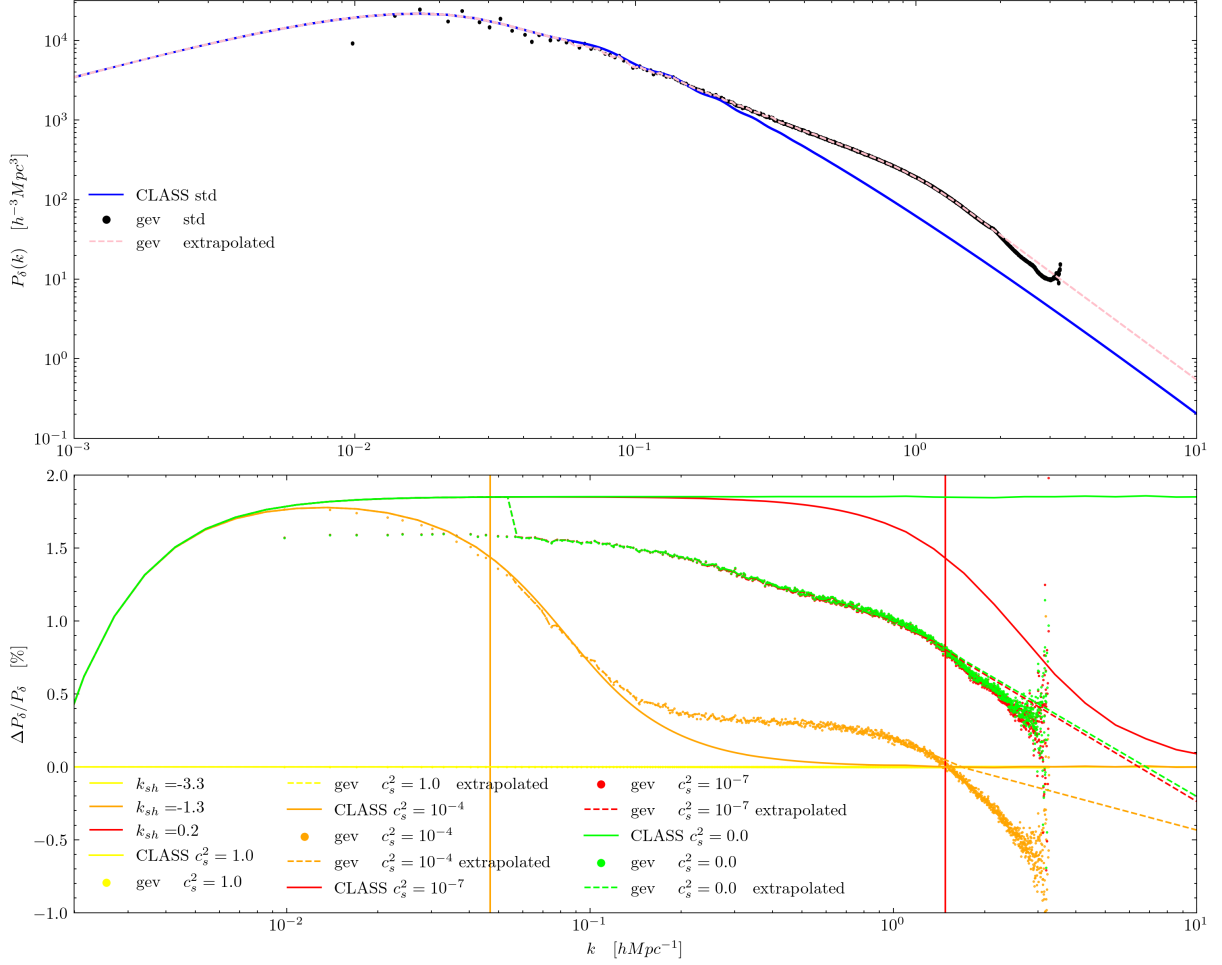


Figure 2: Top panel: matter density power spectrum at redshift $z = 1$. In blue, the linear power spectrum obtain with *CLASS*; in pink, the one interpolated and extrapolated from the *gevolution* runs. Different values of $c_s^2 = 1, 10^{-4}, 10^{-7}, 0$ make no visible difference in this plot. Bottom panel: percentage difference between density power spectra with respect to $c_s^2 = 1$, at redshift $z = 1$. $k_{sh} = 2\pi/\chi_{sh}$ is the sound horizon for each different sound speed.

4.2 boxsize test

By increasing the `boxsize`, we were able to probe the behavior at lower values of k . This way we can hope to determine whether the anomaly we see in Figure 2 is due to a lack of computational power or an actual feature of the plots due to non linear effects.

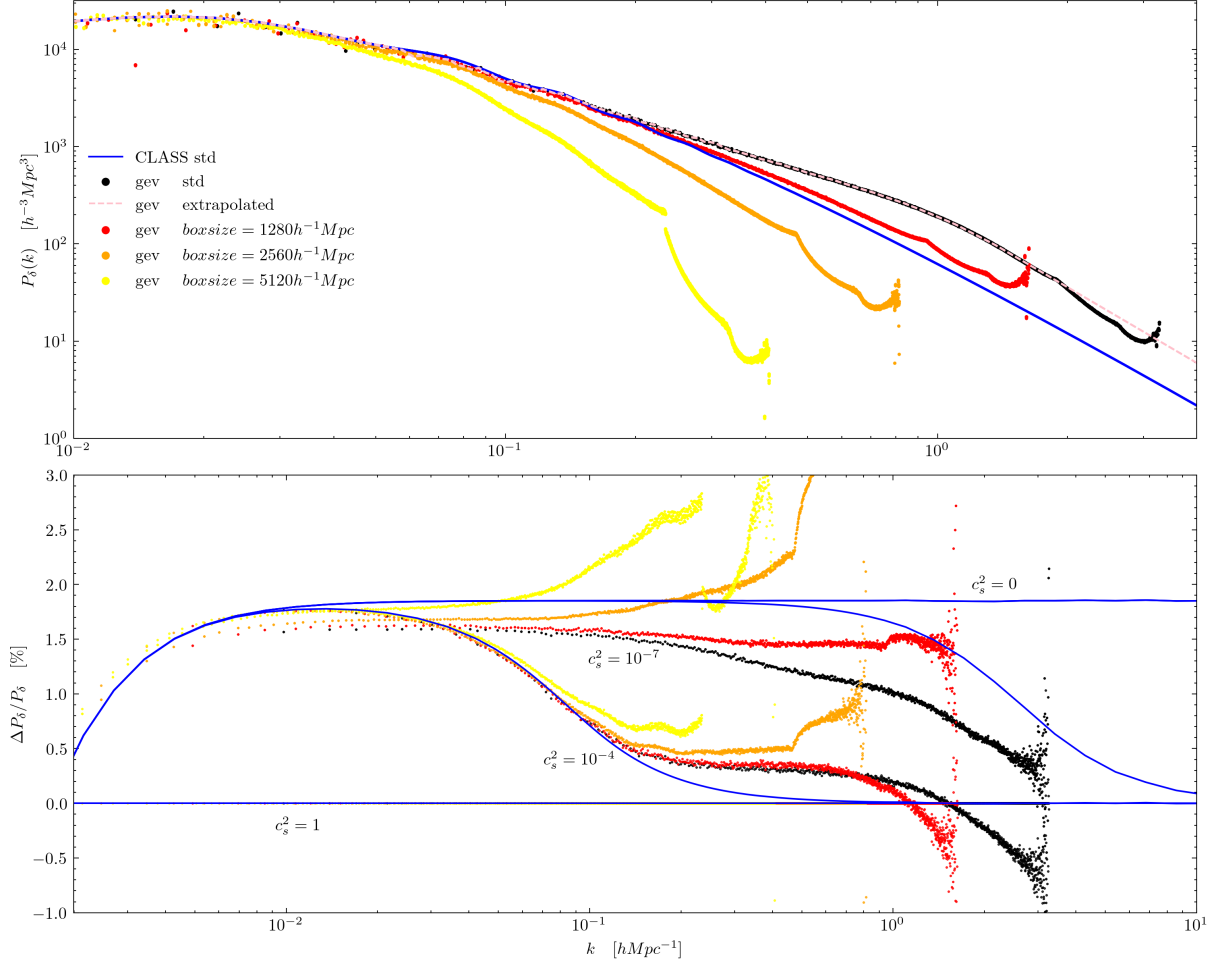


Figure 3: Top panel: power spectra comparison with a gradual increase in `boxsize`. Bottom panel: plot shows the effect of an increase in `boxsize` in the percentage difference plots for each sound speed. The same colour coding as before is used, from smaller `boxsize` (red) to bigger `boxsize` (yellow).

The top panel of Figure 3 shows the non linear power spectra fall below the linear one due to an increasingly lower resolution of the simulation. This drop in resolution is due to the fact that while the `boxsize` is increased, all other parameters are kept constant leading inevitably to a coarser resolution. This also explains why the Nyquist frequency is at lower k for each increase in the `boxsize`. Nevertheless this fall out shouldn't effect the nature of the test for two reasons: firstly, it is only prominent for larger k 's, but we are interested to probe what happens at lower k 's; secondly, the percentage difference plots are obtained with respect to the $c_s = 1$ power spectra for each `boxsize`, therefore the effect should cancel out.

The bottom panel of Figure 3 shows the effects of an increase in `boxsize` for each sound speed. The blue plots are made with *CLASS* and they are the same as in the bottom panel of Figure 2. The effect of an increasing `boxsize` is visually facilitated by the colour coding used, indicating an increase in `boxsize` with cooler colours. It is still hard to say much about the plateau for $c_s^2 = 10^{-4}$ in the bottom panel of Figure 3, since it happens at larger k 's, but it does suggest that plots should follow *CLASS* at lower k 's as the gap between *CLASS* and *gevolution* for $c_s^2 = 10^{-7}$ is closing with an increase in `boxsize`. As a matter of fact, the yellow plot with `boxsize` = $5120h^{-1}Mpc$ for $c_s^2 = 10^{-7}$ has a discrepancy of less than 0.1% for k 's lower than 10^{-1} .

4.3 Correlation function

The correlation function have been obtained by performing the following integral with *Wolfram Mathematica*, using equation (10):

$$\xi(r) = \frac{1}{2\pi^2} \int_0^{+\infty} dk k^2 P(k) \frac{\sin(kr)}{kr}. \quad (10)$$

Proof of the formula can be found in the appendix sections 6.2 and 6.3. For an intuitive explanation of the relation between $\xi(r)$ and $P(k)$, see (Bernardeau et al., 2001).

The non linear matter correlation function in the top panel of Figure 4 does show the main features we expect it to show. The small peak a low r 's, due to a higher clustering of non linear models at small scales. The BAO peak around $r = 100h^{-1}Mpc$.

Finally we can examine the implication that having a sound speed $c_s^2 \ll 1$ has on the non linear correlation function. As the effects are fairly small, hard to notice in the top panel of Figure 4, we examine percentage difference plots in the bottom panel. The feature present around $r = 120h^{-1}Mpc$ is purely mathematical; it arises because the correlation function crosses the x-axis around that length, and due to the nature of the formula

$$\Delta\xi/\xi = 100 \frac{\xi_{c_s^2=1} - \xi_{c_s^2=10^{-4}, 10^{-7}, 0}}{\xi_{c_s^2=1}}, \quad (11)$$

this creates a singularity around the crossing. Below such length we can see again that for $c_s^2 = 10^{-4}$ the *gevolution* follows *CLASS* closely with around 1% noise. For $c_s^2 = 10^{-7}, 0$ instead, we definitely see a closer relation between *gevolution* and *CLASS* with respect to Figure 2, but still not as close as for $c_s^2 = 10^{-4}$. Furthermore we can notice that the plot for $c_s^2 = 10^{-4}$ never follows $c_s = 0$ as we only show lengths below it's sound horizon.

Where as $c_s^2 = 10^{-7}$ follows $c_s = 0$ perfectly until its sound horizon at $\chi_{sh} = 4.2h^{-1}Mpc$, where it drops towards $c_s = 1$.

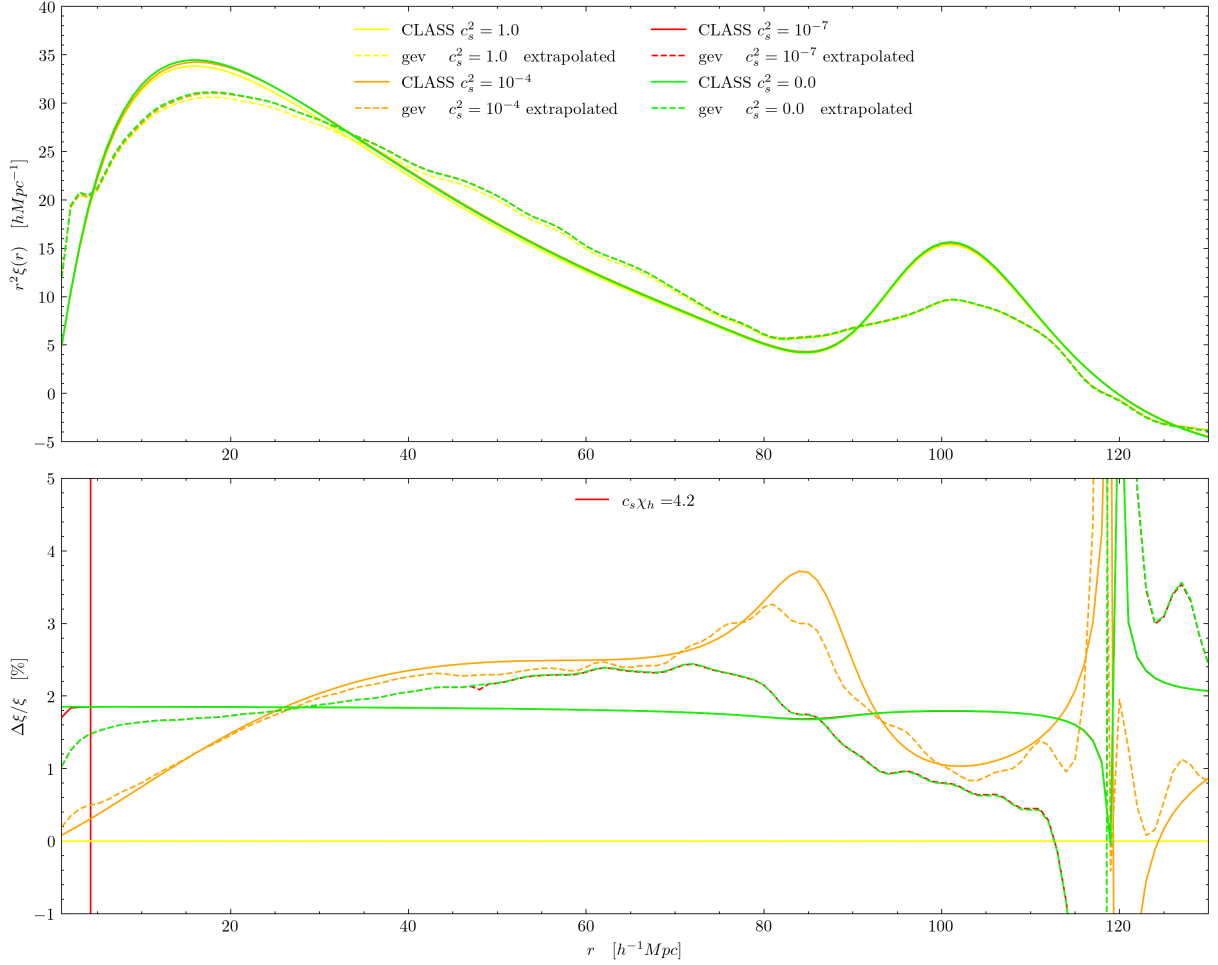


Figure 4: Top panel: matter correlation functions at redshift $z = 1$. The continuous lines are obtained by integrating the linear P_δ . Whereas the dotted lines are obtained by integrating the non linear P_δ obtained with *gevolution*. Bottom panel: percentage difference between correlation functions with respect to $c_s^2 = 1$, at redshift $z = 1$.

5 Conclusion

The main objective of this report was to explore the discrepancy between linear and non linear cosmological structure formation with respect to the effects of a varying sound speed for dark energy. Overall plots deviate from $c_s = 1$ depending on their sound speed, for the power spectra it is always less than 2%, whereas for the correlation functions they sometimes deviate up to 4%. After comparing results found with *CLASS* for the linear

evolution, and *gevolution* for the non linear, we can conclude that power spectra for *gevolution* deviate at most around 1% from CLASS, same for the correlation functions with deviation peaks just above 1% depending on r . In order to determine with more accuracy whether the non linear models differ from linear ones we would need to run *gevolution* simulations at a higher resolution. The data presented in this report does however point towards an equivalence between the two cases, as explained in detail at the end of section 4.2 for matter power spectra and in section 4.3 for their respective correlation functions.

As observations today do not provide strong constraints on sound speed of dark energy, research on models with $c_s^2 \neq 1$ (e.g. k-essence) (Hassani et al., 2023) is still very much available. Still with better constraints in the future, we hope to close in more accurately on a value for the dark energy sound speed.

I would like to thank my external supervisors Prof. Julian Adamek and PhD Francesca Lepori at UZH for the opportunity to work with them, granting this project and guiding me towards its completion. I would also like to thank Prof. Lavinia Heisenberg for being my internal supervisor at ETH.

6 Appendix

6.1 Comoving distance

$$\begin{aligned}\chi &= \int_{r_1}^{r_0} \frac{dr_{phys}}{a} = \int_{t_1}^{t_0} \frac{cdt}{a} = c \int_{a_1}^{a_0} \frac{da}{a\dot{a}} \\ &= c \int_a^1 \frac{da}{a^2 H(a)} = -c \int_z^0 \frac{dz}{H(z)} = c \int_0^z \frac{dz}{H(z)}\end{aligned}\tag{12}$$

where we used the substitution $a = \frac{1}{1+z}$ and $da = -(\frac{1}{1+z})^2 dz = -a^2 dz$.

6.2 $\xi(r)$ as Fourier Transform of $P(k)$ assuming $\xi(r)$ independent of \hat{r}

Relation between the correlation function $\xi(r)$ and the Fourier transformation of the power spectrum function $P(k)$

$$\xi(r) = \frac{1}{(2\pi)^3} \int d^3\vec{k} P(k) e^{i\vec{k}\cdot\vec{r}} \doteq \frac{1}{2\pi^2} \int dk k^2 P(k) \frac{\sin(kr)}{kr}\tag{13}$$

Proof.

$$\xi(r) = \frac{1}{(2\pi)^3} \int d^3\vec{k} P(k) e^{i\vec{k} \cdot \vec{r}} \quad (14)$$

$\xi(r)$ only depends on r and not on the direction of \vec{r} , therefore we can choose $\vec{r} = r\hat{\mathbf{z}}$

$$\xi(r) = \frac{1}{(2\pi)^3} \int d^3\vec{k} P(k) e^{ik_z r}.$$

Spherical coordinate substitution,

$$k_x = k \sin(\theta) \cos(\phi)$$

$$k_y = k \sin(\theta) \sin(\phi)$$

$$k_z = k \cos(\theta)$$

which implies

$$d^3\vec{k} = k^2 \sin(\theta) dk d\theta d\phi.$$

$$\begin{aligned} \xi(r) &= \frac{1}{(2\pi)^3} \int_{-\pi}^{\pi} d\phi \int dk k^2 P(k) \int_0^{\pi} d\theta \sin(\theta) e^{ikr \cos(\theta)} \\ &= \frac{1}{(2\pi)^3} 2\pi \int dk k^2 P(k) \int_0^{\pi} d\theta \sin(\theta) e^{ikr \cos(\theta)} \\ &= \frac{1}{4\pi^2} \int dk k^2 P(k) \int_0^{\pi} d\theta \sin(\theta) e^{ikr \cos(\theta)}. \end{aligned}$$

Substitute,

$$u = \cos(\theta)$$

$$du = -\sin(\theta) d\theta$$

$$u(0) = 1, \quad u(\pi) = -1,$$

The integral simplifies into,

$$\begin{aligned} \xi(r) &= \frac{1}{4\pi^2} \int dk k^2 P(k) \int_1^{-1} -du e^{ikru} \\ &= \frac{1}{4\pi^2} \int dk k^2 P(k) \int_{-1}^1 du e^{ikru} \end{aligned}$$

with,

$$\begin{aligned} \int_{-1}^1 du e^{ikru} &= \frac{1}{ikr} \{e^{ikr} - e^{-ikr}\} \\ &= \frac{1}{ikr} \{\cos(kr) + i \sin(kr) - \cos(kr) + i \sin(kr)\} \\ &= \frac{2 \sin(kr)}{kr}. \end{aligned}$$

Finally,

$$\xi(r) = \frac{1}{2\pi^2} \int dk k^2 P(k) \frac{\sin(kr)}{kr}. \quad (15)$$

□

6.3 $\xi(r)$ as Fourier Transform of $P(k)$ without assuming $\xi(r)$ independent of \hat{r}

Alternative proof without assuming ξ independent from the direction of \vec{r}

Proof.

$$\xi(r) = \frac{1}{(2\pi)^3} \int d^3\vec{k} P(k) e^{i\vec{k} \cdot \vec{r}} \quad (16)$$

plane-wave expansion in spherical harmonics

$$e^{i\vec{k} \cdot \vec{r}} = \sum_{l=0}^{\infty} (2l+1) i^l j_l(kr) \mathcal{P}_l(\vec{k} \cdot \vec{r}), \quad (17)$$

where for the *spherical-harmonic addition theorem*

$$\mathcal{P}(\vec{k} \cdot \vec{r}) = \frac{4\pi}{2l+1} \sum_{m=-l}^l Y_{lm}(\hat{\mathbf{k}}) Y_{lm}^*(\hat{\mathbf{r}}), \quad (18)$$

therefore

$$e^{i\vec{k} \cdot \vec{r}} = 4\pi \sum_{l=0}^{\infty} (2l+1) i^l j_l(kr) \sum_{m=-l}^l Y_{lm}(\hat{\mathbf{k}}) Y_{lm}^*(\hat{\mathbf{r}}). \quad (19)$$

Equation (16) becomes

$$\begin{aligned} \xi(r) &= \frac{1}{(2\pi)^3} \int d^3\vec{k} P(k) 4\pi \sum_{l=0}^{\infty} (2l+1) i^l j_l(kr) \sum_{m=-l}^l Y_{lm}(\hat{\mathbf{k}}) Y_{lm}^*(\hat{\mathbf{r}}) \\ &= \frac{1}{2\pi^2} \int d^3\vec{k} P(k) \sum_{l=0}^{\infty} (2l+1) i^l j_l(kr) \sum_{m=-l}^l Y_{lm}(\hat{\mathbf{k}}) Y_{lm}^*(\hat{\mathbf{r}}). \end{aligned} \quad (20)$$

Using the orthogonality of $Y_{lm}(\hat{\mathbf{k}})$ and $Y_{lm}^*(\hat{\mathbf{r}})$,

$$\int d\Omega_k Y_{lm}(\hat{\mathbf{k}}) Y_{l'm'}^*(\hat{\mathbf{k}}) = \delta_{ll'} \delta_{mm'} \quad (21)$$

which simplifies with $l' = m' = 0$ and $Y_{00}(\hat{\mathbf{k}}) = \frac{1}{\sqrt{4\pi}}$ in

$$\frac{1}{\sqrt{4\pi}} \int d\Omega_k Y_{lm}(\hat{\mathbf{k}}) = \delta_{l0} \delta_{m0}. \quad (22)$$

Spherical coordinates change,

$$\begin{aligned} d^3\vec{k} &= k^2 dk d\Omega_k, \\ \xi(r) &= \frac{1}{2\pi^2} \int dk k^2 P(k) \sum_{l=0}^{\infty} (2l+1) i^l j_l(kr) \sum_{m=-l}^l \int d\Omega_k Y_{lm}(\hat{\mathbf{k}}) Y_{lm}^*(\hat{\mathbf{r}}). \end{aligned} \quad (23)$$

$Y_{lm}^*(\hat{\mathbf{r}})$ is independent from $\hat{\mathbf{k}}$ therefore we can take it out of the integral and apply identity (22)

$$\begin{aligned}
\xi(r) &= \frac{1}{2\pi^2} \int dk k^2 P(k) \sum_{l=0}^{\infty} (2l+1) i^l j_l(kr) \sum_{m=-l}^l Y_{lm}^*(\hat{\mathbf{r}}) \int d\Omega_k Y_{lm}(\hat{\mathbf{k}}) \\
&= \frac{1}{2\pi^2} \int dk k^2 P(k) \sum_{l=0}^{\infty} (2l+1) i^l j_l(kr) \sum_{m=-l}^l Y_{lm}^*(\hat{\mathbf{r}}) \sqrt{4\pi} \delta_{l0} \delta_{m0} \\
&= \frac{1}{2\pi^2} \int dk k^2 P(k) \sum_{l=0}^{\infty} (2l+1) i^l j_l(kr) Y_{l0}^*(\hat{\mathbf{r}}) \sqrt{4\pi} \delta_{l0} \\
&= \frac{1}{2\pi^2} \int dk k^2 P(k) j_0(kr) Y_{00}^*(\hat{\mathbf{r}}) \sqrt{4\pi}.
\end{aligned}$$

Note now that $Y_{00}^*(\hat{\mathbf{r}})$ is simply $1/\sqrt{4\pi}$, which doesn't depend on $\hat{\mathbf{r}}$ anymore. Therefore our angle dependency on $\hat{\mathbf{r}}$ vanishes and we end up with

$$\xi(r) = \frac{1}{2\pi^2} \int dk k^2 P(k) j_0(kr). \quad (24)$$

which is equivalent to the previous result (15), for $j_0(kr)$ is the zeroth spherical Bessel Function and has form $\sin(kr)/kr$. \square

References

- J. Adamek, D. Daverio, R. Durrer, and M. Kunz. General relativity and cosmic structure formation. *Nature Physics*, 12(4):346–349, 2016. URL <https://doi.org/10.1038/nphys3673>.
- R. C. Batista. *A Short Review on Clustering Dark Energy*. 2021. URL <https://doi.org/10.3390/universe8010022>.
- F. Bernardeau, S. Colombi, E. Gaztanaga, and R. Scoccimarro. *Large-Scale Structure of the Universe and Cosmological Perturbation Theory*. 2001. URL <https://doi.org/10.48550/arXiv.astro-ph/0112551>.
- R. de Putter, D. Huterer, and E. V. Linder. *Measuring the Speed of Dark: Detecting Dark Energy Perturbations*. 2010. URL <https://doi.org/10.48550/arXiv.1002.1311>.
- F. Hassani, J. Adamek, and M. Kunz. *Clustering dark energy imprints on cosmological observables of the gravitational field*. 2023. URL <https://arxiv.org/abs/2007.04968>.
- J. Lesgourgues. *The Cosmic Linear Anisotropy Solving System (CLASS) I: Overview*. 2011. URL <https://doi.org/10.48550/arXiv.1104.2932>.

Planck Collaboration. *Planck 2015 results, XIV. Dark energy and modified gravity*. 2016.

URL <https://doi.org/10.1051/0004-6361/201525814>.